

Design, Control, and Experimentation of Internally-Actuated Rovers for the Exploration of Low-Gravity Planetary Bodies

B. Hockman, A. Frick, I.A.D. Nesnas and M. Pavone

Abstract In this paper we discuss the design, control, and experimentation of internally-actuated rovers for the exploration of low-gravity (micro-g to milli-g) planetary bodies, such as asteroids, comets, or small moons. The actuation of the rover relies on spinning three *internal* flywheels, which allows all subsystems to be packaged in one sealed enclosure and enables the platform to be minimalistic, thereby reducing its cost. By controlling the flywheels' spin rates, the rover is capable of achieving large surface coverage by attitude-controlled hops, fine mobility by tumbling, and coarse instrument pointing by changing orientation relative to the ground. We discuss the dynamics of such rovers, their control, and key design features (e.g., flywheel design and orientation, geometry of external spikes, and system engineering aspects). The theoretical analysis is validated on a first-of-a-kind 6 degree-of-freedom (DoF) microgravity test bed, which consists of a 3 DoF gimbal attached to an actively controlled gantry crane.

1 Introduction

The exploration of small Solar System bodies (such as comets, asteroids, or irregular moons) has become a central objective for planetary exploration [1, 2]. In fact, recent ground- and space-based observations indicate that the exploration of small bodies would collectively address all three main science objectives prioritized by NASA's

B. Hockman (✉) · M. Pavone
(Project PI) Department of Aeronautics and Astronautics,
Stanford University, Stanford, CA, USA
e-mail: bhockman@stanford.edu

M. Pavone
e-mail: pavone@stanford.edu

A. Frick · I.A.D. Nesnas
Jet Propulsion Laboratory, California Institute of Technology, Pasadena, CA, USA
e-mail: andreas.frick@jpl.nasa.gov

I.A.D. Nesnas
e-mail: issa.a.nesnas@jpl.nasa.gov

recent decadal survey: (1) the characterization of the early Solar System history, (2) the search for planetary habitats, and (3) an improved understanding about the nature of planetary processes [1]. While measurements of some chemical and physical properties can be obtained by remote sensing from space telescopes or orbiters, measurements that constrain composition (e.g., origin science) and measurements of physical properties that fill strategic knowledge gaps for human exploration require direct contact with the surface at multiple locations for extended time periods [2]. Accordingly, *controlled* mobility in low-gravity environments (micro-g to milli-g) has been identified by the National Research Council in 2012 as one of NASA's high priorities for technology development [3].

Microgravity mobility is challenging due to the virtual absence of traction. A number of approaches to mobility have been proposed in the past two decades, which can be roughly divided into four classes: mobility via thrusters, wheels, legs, and hopping. Thrusters have a number of disadvantages for mobility, including mechanical and operational complexity, limited lifetime (due to propellant limitation), and potential for surface contamination. Wheeled vehicles rely on surface normal forces to create lateral traction—a force that is orders of magnitude weaker in microgravity environments. As a result, wheeled systems are bound to extremely low speeds (1.5 mm/s per previous JPL studies [4]) and can easily lose contact with the surface when traversing rocky terrain, resulting in uncontrollable tumbling. Legged systems rely on anchoring devices at the tips, which are mechanically complex and highly dependent on (largely unknown) surface properties (the challenge of anchoring on a small body has been well illustrated by the recent Philae's landing on a comet [5, 6]). Alternatively, *hopping* systems use the low-gravity environment to their advantage. Space agencies such as NASA [4, 7], RKA [8], ESA [9], and JAXA [10] have all recognized this advantage and have designed a number of hopping rovers. However, existing platforms do not appear to allow precise traverses to designated targets in low gravity environments, as required for targeted in-situ sampling.

Statement of Contributions: In this paper we discuss our ongoing efforts toward the design of a microgravity rover aimed at controlled mobility. The platform uses internal actuation (three mutually-orthogonal flywheels) to generate reaction torques, enabling directional hopping capabilities. Specifically, by applying a controlled *internal* torque between the flywheels and the platform, one generates an angular rotation of the platform. In turn, this angular rotation gives rise to surface reaction forces at external contact points, which lead to either tumbling (i.e., pivoting around a spike tip) or hopping (when the reaction forces are large enough), as shown in Fig. 1, left. External spikes protect the platform during ground collisions and provide the primary contact interface with the surface (see Fig. 1, right). With this design, all subsystems are packaged in one sealed enclosure, which enables the platform to be minimalistic and drastically reduces its cost. Henceforth, we will refer to such a rover as *spacecraft/rover hybrid* (S/R hybrid), since it leverages flywheel actuation (typically used for spacecraft attitude control) for rover mobility.

This paper builds upon a number of previous results on microgravity internal actuation, namely [10], which first proposed the use of internal actuation (specifically a single flywheel mounted on a turntable for limited motion control), and [11, 12],

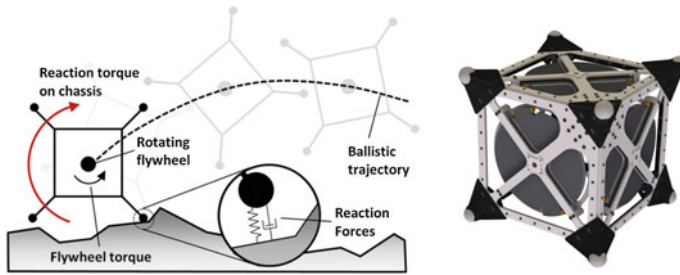


Fig. 1 *Left* By rotating internal flywheels, surface reaction forces make the rover tumble/hop. *Right* Our current prototype without avionics, covers, or solar panels. The cubical structure encloses three flywheels and is protected by external spikes on each of its corners

which consider a torque-controlled three-flywheel configuration and present experimental results on 3 degree-of-freedom (DoF) test beds. This paper is also related to [13], which considers the problem of balancing a cubic body on a corner by actuating three orthogonal flywheels.

Specifically, the contributions of this paper are threefold. First, we characterize the dynamics of the platform and develop hybrid control algorithms for precise mobility (Sect. 2). Our approach leverages a conservation of angular momentum argument, as opposed to the energy approach in [11] used to characterize hopping maneuvers. Second, in Sect. 3 we discuss the mobility platform design, with a focus on *impulsive* actuation of the flywheels to generate more efficient hopping/tumbling maneuvers as compared to [11], and present a preliminary system architecture design. Third, we validate models and control algorithms on a first-of-a-kind 6 DoF microgravity test bed in Sect. 4. The test bed consists of a 3 DoF gimbal attached to an actively controlled gantry crane, and represents, on its own, a major step toward characterizing and validating microgravity mobility (previous test beds only allowed 3DoF tests, e.g., Atwood machine [12], or only allowed tests of the first phases of motion, e.g., parabolic flights and drop towers [14]).

2 Dynamics and Control

In this section we study the dynamics and control of a S/R hybrid by considering a 2D model, i.e., the platform is modeled as a disk with equispaced rigid spikes attached to it, similar to the model commonly used in the field of passive dynamic walking [15]. At the center of mass, a motor drives a single flywheel, producing a torque on the platform (see Fig. 2). A 2D model allows us to derive useful analytical guidelines for actuation and represents a reasonable approximation for 3D configurations in which the S/R hybrid pivots about a pair of spikes.

Our analysis extends earlier studies for this class of rovers (chiefly, [11, 12]) along a number of dimensions. First, our analysis is based on a conservation of angular

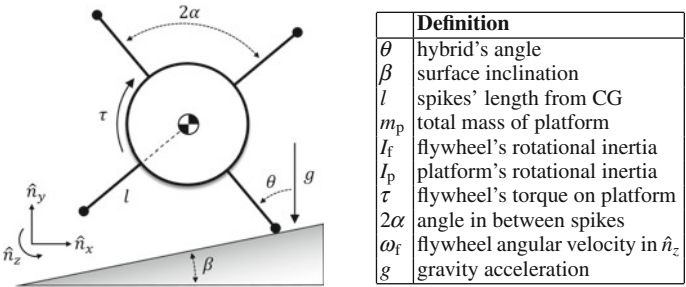


Fig. 2 2D model: A S/R hybrid is modeled as a rigid body that pivots on an inclined surface

momentum argument, which directly accounts for energy losses. In contrast, [11, 12] mostly rely on an energy conservation approach, which, as we will show in Sect. 2.1.1, can lead to gross underestimates in required flywheel actuation. Second, we study the effect of an inclined surface. Third, and perhaps most importantly, we study in detail control strategies for the flywheel.

2.1 Dynamics of S/R Hybrids

A S/R hybrid is essentially capable of two modes of mobility: tumbling and hopping. The key assumption in our study is that the stance spike acts as a pin joint and does not slip. Under this assumption, the 2D model of a S/R hybrid is uniquely described by two states, θ and $\dot{\theta}$. See Fig. 2 for a detailed description of all parameters. A detailed study of the transition between pivoting and sliding motion of the spike tip can be found in [12] for a Coulomb friction model. One can show that modeling the spike tip as a pin joint is a reasonable approximation for coarse spike geometries where $(\theta - \beta) > \tan^{-1}(1/\mu_d)$, where μ_d is the coefficient of dynamic friction. For the rubber spike tips on our current prototype, $1 < \mu_d < 1.5$, which, as validated via simulations in Sect. 2.2, is high enough to justify this no-slip assumption. This assumption, however, would not hold in cases where the hybrid operates on non-rigid surfaces (i.e., loose regolith), whereby the slip properties are governed by frictional interactions with granular media. This aspect is left for future research.

2.1.1 Hopping

A hopping maneuver consists of a stride phase, when the system is supported by a single stance spike, and a flight phase when the stance spike leaves the ground. We study the flywheel's torque needed to cause the platform to hop to the right at a desired speed v_h and angle θ_h (the subscript “h” denotes quantities evaluated at the hopping instant). Assume that the platform starts at rest on the inclined surface and

applies a sufficient clockwise torque $\tau(t)$ that causes it to rotate about its stance spike. For the stride phase (i.e., before ground contact is lost), the equations of motion are those of an inverted pendulum and can be easily written as

$$\ddot{\theta}(t) = \frac{m_p g l \sin(\theta(t)) - \tau(t)}{I_p + m_p l^2}, \quad (1)$$

as also derived in [11]. By studying the free body diagram of the system, one can readily show that in order to obtain a negative normal force (i.e., loss of ground contact) it is required that

$$|\dot{\theta}(t_h)| > \sqrt{\frac{m_p g \cos(\beta) + \frac{\tau(t_h)}{l} \sin(\theta(t_h) - \beta)}{m_p l \cos(\theta(t_h) - \beta)}}. \quad (2)$$

For a flat terrain (i.e., $\beta \rightarrow 0$) and with no input torque, $|\dot{\theta}(t_h)|_{\min} = \sqrt{g/[l \cos(\theta(t_h))]}$, which corresponds to a hop distance on the order of $2l$.

Due to its simplicity, a control strategy of particular interest involves instantaneous momentum transfer from the flywheel to the platform (e.g., via impulsive braking). By equating the initial angular momentum of the flywheel $I_f \omega_f$ to the resulting angular momentum of the platform about the spike tip $\dot{\theta}(I_p + m_p l^2)$, and assuming that a hop is initiated immediately after momentum transfer (i.e., $v_h = l\dot{\theta}(0^+)$), the resulting hop velocity, angle, and lateral distance are given by, respectively,

$$v_h = l\omega_f \left(\frac{I_f}{I_p + m_p l^2} \right), \quad \theta_h = \alpha + \beta, \quad d_h = \frac{v_h^2}{g} \sin(2\theta_h). \quad (3)$$

A few interesting observations can be made from these results. First, in this regime, the hop angle is governed exclusively by the spike geometry and surface inclination. To maximize the lateral distance of the parabolic trajectory (which scales as $\sin(2\theta_h)$), a 45° hop is desired. This is one of the reasons why our current prototype is a cube (i.e., $\alpha = 45^\circ$), see Sect. 3. Second, we define the energy transfer efficiency as

$$\eta := \frac{E(t^+)}{E(t^-)} = \frac{I_f}{I_p + m_p l^2}, \quad (4)$$

where $E(t^-)$ is the energy of the system just before actuation (flywheel kinetic energy), and $E(t^+)$ is the energy just after actuation (platform kinetic energy). Interestingly, the efficiency is given by the ratio of flywheel inertia to platform inertia *about the spike tip*, which depends quadratically on the length of the spikes. Hence, there is an important trade-off between the capability of negotiating obstacles (that would require long spikes) and the actuation efficiency (that prefers short spikes). For our current prototype (augmented with dead mass as stand-in for scientific payload), $\eta \approx 0.01$. This result is critically enabled by angular momentum arguments.

2.1.2 Tumbling

The goal of a tumbling maneuver is to cause the platform to pivot to the right and land on the next consecutive spike such that its orientation is incremented by -2α and that it does not lose contact with the surface. From (1), the minimum torque required to initiate angular acceleration ($-\ddot{\theta}$) from rest on the surface is given by

$$\tau_{\min} = m_p g l \sin(\alpha + \beta). \quad (5)$$

For typical gravity levels of interest ($10\text{--}1000\mu\text{g}$), small motors of only a few Watts would be sufficient to exceed this torque. To characterize actuation bounds for tumbling, the actuation is regarded as an instantaneous transfer of momentum, similar to the hopping analysis in Sect. 2.1.1. Accordingly, the initial kinetic energy of the platform at $t = 0^+$ can be equated to the gravitational potential energy at the tumbling apex ($\theta = 0$). This yields an expression for the *minimum* flywheel velocity required to vault the platform over its leading spike: $\omega_{f, \min} = \sqrt{2m_p g l (1 - \cos(\alpha + \beta)) / (\eta I_f)}$. Note that a similar result is provided in [11], but it does not directly account for energy losses or accommodate inclined surfaces. This leads to an underestimate of control input by a factor of $1/\sqrt{\eta} \approx 10$, thus illustrating the importance of an angular momentum approach.

To characterize the *maximum* flywheel velocity for tumbling, consider the hop criterion given by (2) and a zero torque input for $t \geq 0^+$. It follows that $\theta(t)$ and $|\dot{\theta}(t)|$ both decrease with time. Thus, if surface contact is lost, it will occur just after momentum transfer when $\theta(0^+) = \alpha + \beta$, and $|\dot{\theta}(0^+)| = \eta\omega_f$. This yields the maximum flywheel velocity to perform a tumble without hopping: $\omega_{f, \max} = \sqrt{[g \cos(\beta)] / [\eta^2 l \cos(\alpha)]}$. Interestingly, there exists an inclination angle, β_{\max} , for which $\omega_{f, \min} = \omega_{f, \max}$ and tumbling is impossible. For a square geometry ($\alpha = 45^\circ$), $\beta_{\max} \approx 30^\circ$. Also, as expected, $\omega_{f, \min} = 0$ when $\beta = -\alpha$, which corresponds to the declination angle at which the platform freely tumbles “downhill” without actuation.

2.2 Control of S/R Hybrids

In this section, we study a control strategy that leverages (5) by slowly spinning up the flywheels with motor torque $\tau < \tau_{\min}$, such that the platform remains grounded. When the desired flywheel speed is achieved, a brake is applied and a hop is initiated as discussed in Sect. 2.1.1. This approach is attractive as it is simple, does not cause momentum build up in the flywheels, and generates high torques for larger hops.

With this control strategy, one can regard the initial flywheel speed ω_f and constant braking torque $\bar{\tau}$ as the two control variables. In bringing the flywheel to a full stop, the control variables are related by $\bar{\tau} \Delta t = I_f \omega_f$, where Δt is the time duration of braking. In the limit as $\Delta t \rightarrow 0$, the impulsive torque corresponds to the case of instantaneous momentum transfer discussed in Sect. 2.1, whereby Eqs. (3) and (4)

can be combined to develop an expression for the flywheel speed ω_f required to cover a lateral distance d_h :

$$\omega_f(d_h) = \sqrt{\frac{d_h g}{\eta^2 l^2 \sin(2(\alpha + \beta))}}. \quad (6)$$

For a square geometry, this expression is minimized for flat terrain, but tends towards infinity as $\beta \rightarrow 45^\circ$. This motivates the potential utility of controllable friction brakes, which can extend the duration of the stride phase and thus control the hop angle. To study the case where Δt is finite, the nonlinear differential equations of motion given by (1) must be solved numerically. However, for aggressive hops, one can assume that $\bar{\tau} \gg m_p g l \sin(\theta)$, so (1) can be well approximated by the linear second order ODE, $\ddot{\theta}(t) \approx -\bar{\tau}/(I_p + m_p l^2)$. For high enough torques, the hop criterion in (2) is not met until immediately after actuation (i.e., a hop is induced at $t_h = \Delta t = \omega_f I_f / \bar{\tau}$), so the initial hop state can be determined by integration:

$$\dot{\theta}(t_h) = \frac{-\bar{\tau} t_h}{I_p + m l^2} = \eta \omega_f, \quad \theta(t_h) = \alpha - \frac{\eta I_f \omega_f^2}{2 \bar{\tau}}. \quad (7)$$

Since $\theta(t_h)$ is now a function of ω_f and $\bar{\tau}$, the required torque input requires solving a nonlinear algebraic equation: $d_h = \sin(2\alpha - \eta I_f \omega_f^2 / \bar{\tau}) (\eta l \omega_f)^2 / g$.

To better visualize these results and validate the pivoting assumptions, numerical simulations were generated based on a full 6 DoF model, including normal spring/damper and tangential coulomb friction contact forces (as used in [12]).

The plots in Fig. 3 illustrate the hopping angle and distance relationships. Each plot represents a different flywheel speed (2000, 5000, and 10,000 rpm) and the x -axis is the braking torque $\bar{\tau}$. The kink in each curve marks the threshold of an “early hop”—the torque level $\bar{\tau}_s$ below which surface contact is lost before the flywheel is fully stopped. In other words, for a given flywheel speed, $\bar{\tau}_s$ is the minimum braking torque that should be applied to convert all of the flywheel’s available kinetic energy to forward motion. This threshold (marked by a vertical line) is in very close agreement with predictions based on (2).

Figure 3b shows that for $\beta \leq 0$, travel distance increases as the torque is increased. However, the situation is different when considering inclined poses ($\beta \geq 0$), whereby high torque inputs result in high angle arching hops—an undesirable effect for distance coverage but potentially useful for getting out of pits. The peaks in these distance curves are in agreement with (6).

The duration of a single hopping maneuver can be thought of as the sum of the time to spin up the flywheels (T_{spin}), and the time of flight (T_{flight}), where

$$T_{\text{spin}} = K_S \left(\frac{\sqrt{2} \omega_f I_f}{m_p g l} \right), \quad T_{\text{flight}} = K_B \left(\frac{\sqrt{2} \eta l \omega_f}{g} \right), \quad d_{\text{hop}} = K_D \left(\frac{(\eta l \omega_f)^2}{g} \right). \quad (8)$$

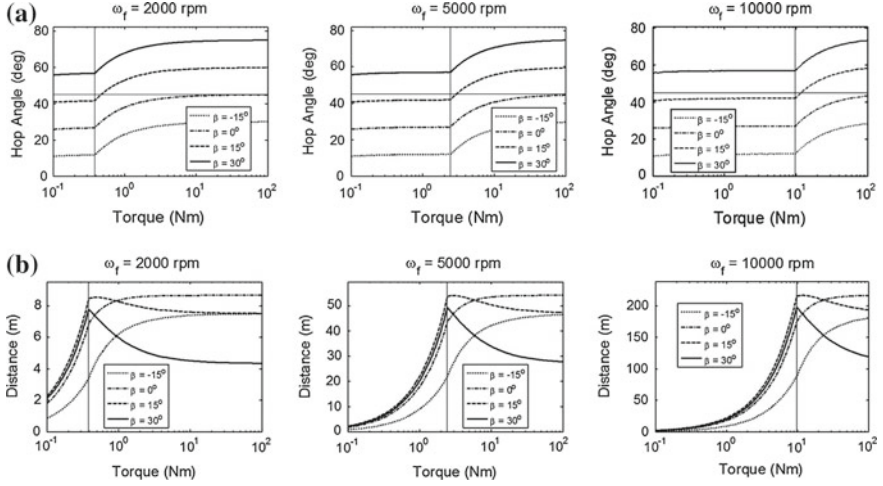


Fig. 3 Resulting hop angles and distances as functions of input torque for three initial flywheel speeds: $\omega_f = 2000, 5000$, and $10,000$ rpm (the x -axis is in logarithmic scale). Each curve corresponds to a particular surface inclination β . The vertical line on each graph marks the minimum torque at which the flywheel can be fully stopped before a hop is initiated (see Eq. (2)). Results are based on Phobos' gravity level (0.0058 m/s^2) and parameters of our prototype (see Sect. 3.1). **a** Hopping angle (θ_h) as a function of input torque ($\bar{\tau}$). The horizontal line marks the 45° “ideal” hop angle. **b** Lateral hop distance (d_h) as a function of input torque ($\bar{\tau}$)

These equations result directly from (1) and (3), and assuming $\theta_{\text{hop}} = \alpha = 45^\circ$. Here, K_S represents a safety factor for tipping during flywheel spin-up, K_B can be thought of as the settling time for residual bouncing as a proportional gain on the parabolic flight time, and K_D is also a proportional gain on hop distance to account for bouncing as well as for deviations in heading. Based on observations from simulations, conservative estimates are $K_B = 2$, and $K_S, K_D = 1.2$. Combining (8) and (6) yields the average expected speed:

$$\bar{V} = \frac{d_{\text{hop}}}{T_{\text{flight}} + T_{\text{spin}}} = \frac{\sqrt{2d_h g}}{2} \left(\frac{K_D \eta m_p l^2}{K_B \eta m_p l^2 + K_S I_f} \right) \approx \frac{\sqrt{2d_h g}}{2} \left(\frac{K_D}{K_B + K_S} \right). \quad (9)$$

The above approximation assumes $I_p + m_p l^2 \approx m_p l^2$, which is reasonable for our prototype ($m_p l^2 = 0.13$ and $I_p = 0.03$). Interestingly, \bar{V} depends on the square root of hop distance and gravity, indicating that farther hops result in faster net motion, and motion on bodies with weaker gravity is slower. On Phobos ($g = 0.0058 \text{ m/s}^2$), with the parameters of our current prototype, the parameters K_S, K_B , and K_D defined above, and for an average 10 m hop, we can expect a net speed of about 7 cm/s. However, for longer excursions, hops of 100 m are reasonable (i.e., $\omega_f = 6000 \text{ rpm}$), and could increase net speed to over 20 cm/s.

3 Prototype Design

3.1 S/R Hybrid Structural Design

The prototype and CAD models for the structure and the flywheels (including the braking mechanism) are shown in Fig. 4. The three mutually orthogonal flywheels are mounted with bearing supports to adjacent internal faces of the cube to maximize their inertia (larger diameter) and allow more space for scientific payload and avionics. Each flywheel is directly driven by a small 2 W brushless DC motor (capable of $\tau_{\max} \approx 10 \text{ mNm}$) and motor controllers. Inspired by the theoretical benefits of high torque capabilities (discussed in Sect. 2.2), an impulsive braking mechanism was implemented, whereby an actuated “impact hammer” mounted to the structure collides with a protruding surface on the flywheel (earlier prototypes utilize, instead, friction brakes [11]). The spring-loaded impact hammers are jointly actuated to retract, allowing the flywheels to freely spin, and simultaneously released to snap into place for braking. An on-board microcontroller coordinates motion and collects data, and the system is powered by a 12 V DC battery. The motors have embedded hall sensors that act as velocity sensors, which can also provide torque information according to the relation $\tau = I_f \alpha_f$.

The overall structure and frame consists of a cube with an 8-in edge constructed out of lightweight laser-cut and 3-D printed parts (see Eq. (4) for motivation behind keeping m_p and I_p low), and one spike on each corner. Previous prototype iterations included more spikes [11], but it has been determined through experimentation and insights from dynamic analysis (see Sect. 2) that a cubic geometry with 8 spikes offers the best balance of protection and mobility performance. Each spike is fitted with a rubber tip to absorb impacts and increase surface friction.

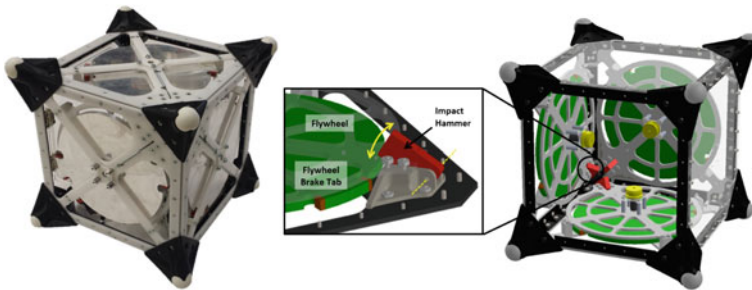


Fig. 4 Prototype and CAD models (not to scale), highlighting the impulsive braking system. The structural parameters are: $m_p = 3.75 \text{ kg}$, $l = 0.17 \text{ m}$, $I_f = 0.95 \text{ g m}^2$, $I_p = 30 \text{ g m}^2$, $\alpha = 45^\circ$

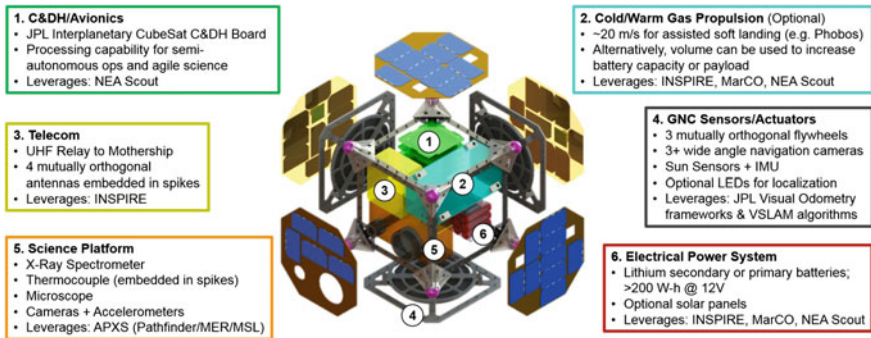


Fig. 5 Preliminary system architecture based on the current prototype design discussed in Sect. 3.1. Key subsystems include: avionics, gas propulsion system, telecommunications, sensors/actuators, power system, and scientific instruments. For the CubeSat mission acronyms, we refer the reader to [16]

3.2 S/R Hybrid System Architecture

Figure 5 shows a preliminary system architecture configuration where most subsystems leverage concurrent CubeSat missions under design at JPL [16] (due to space limitations, we provide here a very brief discussion). Although not required for mobility, space was allocated for a gas propulsion system to facilitate soft landing on deployment from the mothership. The deployment phase is a challenging problem but not the focus of this paper. The power system can incorporate both primary batteries (greater storage density) and secondary batteries that can be recharged by the solar panels. The rest of the space is available for avionics, telecommunication systems, sensors, and of course scientific instruments such as microscopes and an X-Ray Spectrometer (XRS). While this system is built on an 8U package size¹ (same as our current prototype), the platform is *scalable* and could be miniaturized to 1U nano-versions or enlarged for very capable versions up to 27U.

4 Microgravity Test Bed and Experiments

4.1 Test Bed Design

To the best of authors' knowledge, no preexisting test beds are capable of accurately emulating 6 DoF motion within a microgravity environment for an extended period of time (say, more than 20 s) and within an extended workspace (say, more than 1 m²). ARGOS, a gravity offload system developed at NASA's Johnson Space Center, may

¹In CubeSat's jargon, one unit, i.e., 1U, refers to the standard size 10 × 10 × 10 cm volume.

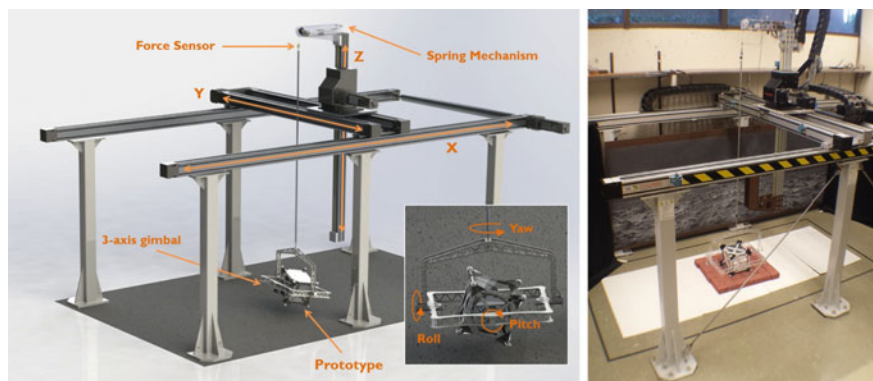


Fig. 6 *Left* 6 DoF microgravity test bed CAD rendering. The powered gantry tracks the translational motion of the platform in x , y , and z within a volume of $3\text{ m} \times 1\text{ m} \times 1\text{ m}$ respectively, while allowing for free fall in z at sub-milli- g levels. The gimbal frame allows the platform to rotate in all three axes. *Right* Image of the test bed

come the closest [17]. Used primarily for human testing in zero- g environments, ARGOS consists of an actively-controlled overhead 3-axis gantry crane that tracks the motion of the suspended subject, enabling the “free-floating” behaviors observed in space. At Stanford, we have extended this idea to create a novel 6 DoF test bed for operating rovers in *microgravity* conditions (see Fig. 6). Similar to ARGOS, this test bed is built on a powered gantry crane that permits the tracking of translational motion.

The 3-axis rotational motion is achieved by mounting the platform within a light-weight rigid gimbal frame (see Fig. 6) (Rigorously, the gimbal only enables 2.5 DoF of rotation because the roll axis is bounded to avoid ground contact with the gimbal itself.). Dead mass is fixed to the platform to geometrically center the CG such that it is precisely aligned with the three rotational axes of the gimbal for free rotation. However, this requirement can be relaxed for operation in true microgravity (i.e., on an asteroid) where the platform is no longer suspended. In this case, the control analysis in Sect. 2.2 can be modified to account for an offset CG. For example, a CG offset from the geometric centroid by 10% of the spike radius would scale the required flywheel speed up by about 20% on one side, and down by 20% on the opposite side.

The gimbal-mounted platform is suspended by a (2 m) cable from an overhead attachment point on the gantry crane so that it can swing freely. By accurately measuring the relative deflection of the pendulum at 100 Hz, the x and y axes are actuated using feedback control techniques to keep the pendulum in a vertical state. In this manner, external lateral forces that act on the platform cause the whole system to accelerate as Newton’s second law predicts. The sensor that performs this measurement is based on the principle of inductive sensing, whereby strategically placed inductive pick-up circuits measure the strength of the AC current-induced magnetic field emitted by the suspension cable (and thus its deflection due to $1/r$ dissipation).

The vertical actuation of the test bed enables microgravity behaviors, yet presents a very difficult engineering challenge. Its role is to apply a finely controlled constant lifting force on the platform equal to 99.9 % of its weight to induce milli-g level free fall. Applying such a precise force is a challenge in its own right, as passive force elements such as springs and bearings have excessive friction and hysteresis, and the noise floor of many force sensors is also on the order of 0.1 %. A precision load cell (4 digit resolution) is mounted along the suspension cable in a feedback configuration with the z -axis control of the gantry to produce the desired free fall accelerations. However, in order to maintain this constant offloading force during impulsive force inputs (i.e., ground collisions), the gantry must also respond immediately and at very high accelerations—a fundamental limitation of the drive motors. The dynamic response for force tracking can be greatly improved by introducing a passive spring element along the pendulum, which behaves like a series elastic actuator—a commonly used technique in robotics for high fidelity force control [18]. A low-stiffness spring/cam pulley system provides this compliance as described in [19].

Since the dynamics of the system in both the lateral and vertical axes can be simplified to an equivalent linear mass/spring/damper system *about the equilibrium*, we use standard PID control. Furthermore, because the pendulum deflections are kept very small (less than 1°), the vertical force feedback is decoupled from lateral cable deflections, allowing for three independent control loops (one for each axis).

4.2 Test Bed Validation

The test bed was validated by performing reference drop and lateral maneuvers. Specifically, drop tests with only vertical actuation exhibit a very strong parabolic fit (correlation typically above 99 %), and the noise floor on the force sensor feedback allows for effective gravity levels down to about 0.0005 g's. The lateral motion also behaves precisely as predicted without force input, remaining stationary or in a constant velocity. However, there is a small amount of drift in the signal from the lateral sensors (roughly 0.0001 g's/min), which is handled with periodic recalibration before experiments. Interestingly, the lateral signal can be intentionally biased to tilt the acceleration vector off vertical, producing an effectively inclined surface.

A more careful analysis is required to validate the test bed's response to external forces, which can be either impulsive or non-impulsive. As a first test, a constant lateral force was applied to the platform (mass m_p) mounted on the test bed with a horizontal string looped over a pulley with a known mass m_t suspended. After initial transients settle, the system tracks the expected acceleration ($a = gm_t/(m_p + m_t)$) to within 5 %. A similar test was performed in the vertical axis by simply adding small amounts of known mass to the platform, which also produces accelerations in close agreement with theoretical predictions (to within 1 %).

Characterizing the behavior under impulsive contact forces is more challenging. First of all, the elasticity of a collision depends on many factors (e.g., properties of contacting materials, speed of impact, geometry of deformation, etc.), making

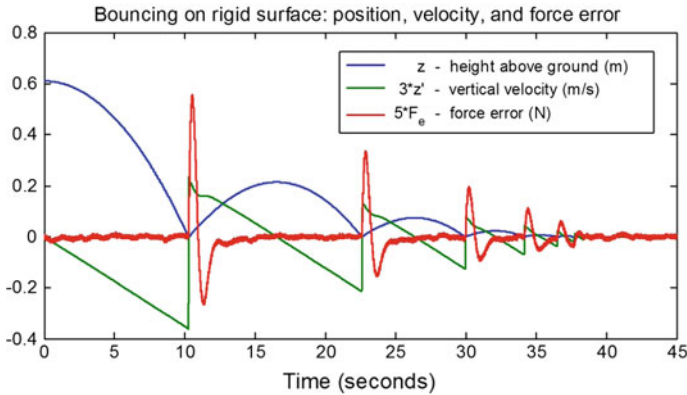


Fig. 7 Experimental results from bouncing on a rigid surface at 0.001 g’s: height and velocity of test mass and error in vertical offloading force. Data is sampled at 10 kHz and the control loop runs at 100 Hz. Note that data is scaled to fit on same axes (see legend for scaling and units)

it impractical to characterize theoretically as a basis for comparison. However, as a preliminary test, a proof mass (equal to the mass of the prototype) was mounted on the test bed and dropped onto an elastic surface (basically a webbing of rubber surgical tubing acting as trampoline)—a contrived, low-stiffness interface that dissipates very little energy. In drop tests at 0.001 and 0.005 g’s, the mass was released from rest a height of roughly 1 m, and it did indeed recover about 90 % of its energy after each subsequent collision (number of trials = 36, mean = 91.5 %, and standard deviation = 2.7 %).

For collisions with stiffer or even rigid surfaces, energy dissipation is much more difficult to predict. However, the deviation observed in the force signal during impact is a good indicator of fidelity. Figure 7 reports the vertical height and velocity of the proof mass during an example drop/bouncing sequence on a rigid surface, as well as the transient force errors. Although the gantry overshoots vertical position by up to a few inches after a collision, the low stiffness of the spring mechanism ($\approx 5 \text{ N/m}$) results in transient force errors less than a few hundred milli-Newtons—less than 1 % of the proof mass’ weight. Since the force error scales roughly linearly with impact speed, there is an upper bound at which the transient response becomes unacceptable, putting the ideal range of operation between 0.0005 and 0.005 g’s.

4.3 Mobility Experiments

To further characterize the dynamics and *controllability* of the hybrid and to asses the validity of the model presented in Sect. 2.1, simple hopping experiments were performed on the test bed discussed in Sect. 4.1. As a first set of experiments, we considered a flat rigid surface and constrained the test bed motion to only two axes

(x and z) for direct comparison with the 2D analysis in Sect. 2.1. The initial platform orientation about the yaw axis is also set such that it is “facing” along the x axis, for stable pivoting about its two leading spikes. In each experiment, we executed the control approach discussed in Sect. 2.2, whereby the flywheel is slowly accelerated until a target angular velocity is reached, at which point the impulsive brakes are applied and the hopping sequence ensues unactuated. For a desired hop distance of 0.75 m in an emulated gravity level of 0.001 g’s, the target flywheel velocity was calculated using (6) to be 700 rpm. The $x/y/z$ position feedback from the gantry was used in conjunction with the force and displacement signals to determine the trajectory of the hybrid in 20 experiments, four of which are plotted in Fig. 8.

An interesting observation from Fig. 8 is the variability in bouncing. Even for constrained 2D motion on a uniform flat surface, bouncing speed and angle are highly dependent on spin and orientation at the instant of impact. On the other hand, hopping angle measurements exhibit a more consistent trend and are in close agreement to the prediction of (7). The mean hop angle for the 20 experiments was 51° with a standard deviation of 4° . This is marginally higher than the 45° prediction likely due to the elastic rebound of the spike tip, which is not accounted for in the theoretical model. Specifically, instead of stopping immediately on impact as assumed in analysis, the flywheel rebounds and strikes the brake in the opposite direction, resulting in an initial hopping torque much higher than expected, shortly followed by a reverse torque. This actually causes the hybrid to counter-rotate immediately after liftoff. This explains why more energy is converted to translational motion and more distant hops than predicted. In fact, based on the 20 experiments, the mean hop distance of 1.27 m is about 70 % farther than intended—a seemingly beneficial effect. However, this presumably comes at the cost of shorter bounces due to counter-rotation. Nonetheless, correcting for hopping angle and distance discrepancies allows for *controlled* hopping with repeatable performance. We note that, although the analysis and experimental results suggest that impulsive brakes are indeed more efficient, they are

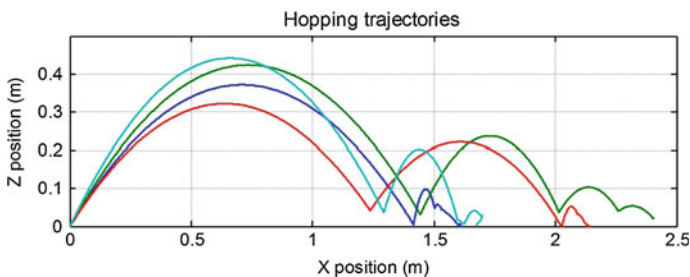


Fig. 8 Hopping trajectories of the hybrid within the microgravity test bed. The gravity level of these experiments was set to 0.001 g’s, and the flywheel was commanded to 700 rpms. Position data for each experiment was shifted to start at the origin. A z position of zero corresponds to a flat stance where four spikes are in contact with the ground. Thus, bounces above zero indicate collision at a tilted orientation

also less controllable than friction brakes and induce high mechanical stresses in the structure. See <http://web.stanford.edu/~pavone/movies/hop.mov> for a sample video of a hopping experiment.

5 Conclusions

In this paper, we presented a planetary mobility platform that uses internal actuation to achieve controlled maneuvers for long excursions (by hopping) and short, precise traverses (by tumbling) in low-gravity environments. We have characterized the dynamics of such platforms using angular momentum arguments and developed hybrid control strategies for precise mobility. We have also presented a preliminary system architecture and prototype design, which has been used to validate control techniques in a first-of-a-kind 6 DoF microgravity test bed. Experimentation is ongoing, but the preliminary results constitute the first successful demonstration of *controlled* hopping mobility in such a high fidelity test bed.

This paper leaves numerous important extensions open for further research. First, it is important to develop more realistic contact models for interactions with loose, granular media typically found on small bodies. Second, we seek to extend the control algorithms to reliably maneuver rocky terrains and leverage them for higher level motion planning objectives. Third, from a navigation perspective, we plan to develop SLAM techniques suited for the unique and challenging environments of small bodies, and for the constantly rotating motion of the platform. Finally, future experiments will include (1) extension to all three axes, with hopping about non-symmetric orientations, (2) various surface characteristics such as inclination, rocks, sand, and fine powder, and (3) tests of the closed-loop system integrating planning, control, and navigation.

Acknowledgments The research described in this paper is supported by NASA under the Innovative Advanced Concepts program, and by the Jet Propulsion Laboratory (JPL) under the R&TD and CAP programs. The authors wish to acknowledge insightful discussions with Dr. J.C. Castillo (JPL), R. Reid (JPL), Dr. C. Zuffada (JPL), Dr. T. Cwik (JPL), Dr. J. Zmuidzinas (JPL), and B. Wilcox (JPL). Government sponsorship acknowledged.

References

1. Decadal Survey Vision and Voyages for Planetary Science in the Decade 2013–2022. Technical report, National Research Council (2011). <http://solarsystem.nasa.gov/2013decadal/>
2. Castillo Rogez, J.C., Pavone, M., Nesnas, I.A.D., Hoffman, J.A.: Expected science return of spatially-extended in-situ exploration at small solar system bodies. In: IEEE Aerospace Conference, pp. 1–15, Big Sky, MT, Mar 2012
3. NASA Space Technology Roadmaps and Priorities: Restoring NASA's Technological Edge and Paving the Way for a New Era in Space. Technical report, National Research Council (2012)

4. Jones, R.M.: The MUSES-CN rover and asteroid exploration mission. In: 22nd International Symposium on Space Technology and Science, pp. 2403–2410 (2000)
5. Glassmeier, K.-H., Boehnhardt, H., Koschny, D., Kührt, E., Richter, I.: The Rosetta mission: flying towards the origin of the solar system. *Space Sci. Rev.* **128**(1–4), 1–21 (2007)
6. Hand, E.: Philae probe makes bumpy touchdown on a comet. *Science* **346**(6212), 900–901 (2014)
7. Fiorini, P., Burdick, J.: The development of hopping capabilities for small robots. *Auton. Robots* **14**(2), 239–254 (2003)
8. Sagdeev, R.Z., Zakharov, A.V.: Brief history of the Phobos mission. *Nature* **341**(6243), 581–585 (1989)
9. Dietze, C., Herrmann, S., Kuß, F., Lange, C., Scharringhausen, M., Witte, L., van Zoest, T., Yano, H.: Landing and mobility concept for the small asteroid lander MASCOT on asteroid 1999 JU3. In: 61st International Astronautical Congress (2010)
10. JAXA Hayabusa mission: Technical report, JAXA (2011). <http://hayabusa.jaxa.jp/e/index.html>
11. Allen, R., Pavone, M., McQuin, C., Nesnas, I.A.D., Castillo Rogez, J.C., Nguyen, T.-N., Hoffman, J.A.: Internally-actuated rovers for all-access surface mobility: theory and experimentation. In: Proceedings IEEE Conference on Robotics and Automation, pp. 5481–5488, Karlsruhe, Germany, May 2013
12. Reid, R.G., Roveda, L., Nesnas, I.A.D., Pavone, M.: Contact dynamics of internally-actuated platforms for the exploration of small solar system bodies. In: i-SAIRAS, pp. 1–9, Montréal, Canada, June 2014
13. Gajamohan, M., Merz, M., Thommen, I., D’Andrea, R.: The Cubli: a cube that can jump up and balance. In: IEEE/RSJ International Conference on Intelligent Robots and Systems, pp. 3722–3727. IEEE (2012)
14. Yoshimitsu, T., Kubota, T., Nakatani, I., Adachi, T., Saito, H.: Microgravity experiment of hopping rover. In: Proceedings of IEEE Conference on Robotics and Automation, vol. 4, pp. 2692–2697 (1999)
15. McGeer, T.: Passive dynamic walking. *Int. J. Robot. Res.* **9**(2), 62–82 (1990)
16. JPL’s Cubesats: Technical report, JAXA (2015). <http://cubesat.jpl.nasa.gov/>
17. Valle, P., Dungan, L., Cunningham, T., Lieberman, A., Poncia, D.: Active Response Gravity Offload System (2011)
18. Jerry, P., Krupp, B., Morse, C.: Series elastic actuators for high fidelity force control. *Ind. Robot: Int. J.* **29**(3), 234–241 (2002)
19. Duval, E.F.: Dual pulley constant force mechanism, 16 Mar 2010. US Patent 7,677,540